ARMY RESEARCH LABORATORY

ARL

A Description of the Framework of the Atmospheric Boundary Layer Environment (ABLE) Model

by Yansen Wang, Chatt Williamson, and Benjamin MacCall

NOTICES

Disclaimers

The findings in this report are not to be construed as an official Department of the Army position unless so designated by other authorized documents.

Citation of manufacturer's or trade names does not constitute an official endorsement or approval of the use thereof.

Destroy this report when it is no longer needed. Do not return it to the originator.

Army Research Laboratory

Adelphi, MD 20783-1197

ARL-TR-6177   **September 2012**

A Description of the Framework of the Atmospheric Boundary Layer Environment (ABLE) Model

Yansen Wang, Chatt Williamson, and Benjamin MacCall
Computational and Information Sciences Directorate, ARL

---

1. REPORT DATE *(DD-MM-YYYY)*	2. REPORT TYPE	3. DATES COVERED (From - To)
September 2012	Final	

4. TITLE AND SUBTITLE	5a. CONTRACT NUMBER
A Description of the Framework of the Atmospheric Boundary Layer Environment (ABLE) Model	
	5b. GRANT NUMBER
	5c. PROGRAM ELEMENT NUMBER

6. AUTHOR(S)	5d. PROJECT NUMBER
Yansen Wang, Chatt Williamson, and Benjamin MacCall	
	5e. TASK NUMBER
	5f. WORK UNIT NUMBER

7. PERFORMING ORGANIZATION NAME(S) AND ADDRESS(ES)	8. PERFORMING ORGANIZATION REPORT NUMBER
U.S. Army Research Laboratory ATTN: RDRL-CIE-D 2800 Powder Mill Road Adelphi, MD 20783-1197	ARL-TR-6177

9. SPONSORING/MONITORING AGENCY NAME(S) AND ADDRESS(ES)	10. SPONSOR/MONITOR'S ACRONYM(S)
	11. SPONSOR/MONITOR'S REPORT NUMBER(S)

12. DISTRIBUTION/AVAILABILITY STATEMENT
Approved for public release; distribution unlimited.

13. SUPPLEMENTARY NOTES

14. ABSTRACT

This technical report documents the framework of a three-dimensional Atmospheric Boundary Layer Environment (ABLE) model. The objective of the project is to develop a microscale boundary layer meteorological model to fill the gap in Army applications. A set of incompressible equations for momentum, energy, and scalar is chosen specifically for the microscale meteorological modeling. A Cartesian coordinate with a structured grid is selected for a fast computation and domain preprocessing. A finite volume numerical method with a collocated grid is applied in this framework. Some planned features for this model system, such as turbulence model for sub-grid scale and the immersed boundary method, are also described briefly. Bench mark test cases compared with the laboratory data and with other numerical simulations are also performed and documented.

15. SUBJECT TERMS

Atmospheric Boundary Layer, Finite Volume method, Microscale Meteorological Model

16. SECURITY CLASSIFICATION OF:			17. LIMITATION OF ABSTRACT	18. NUMBER OF PAGES	19a. NAME OF RESPONSIBLE PERSON Yansen Wang
a. REPORT	b. ABSTRACT	c. THIS PAGE	UU	32	19b. TELEPHONE NUMBER (*Include area code*)
Unclassified	Unclassified	Unclassified			(301) 394-1310

Contents

List of Figures

INTENTIONALLY LEFT BLANK.

1. Introduction

In meteorology, *microscale* phenomena exhibit spatial scales from a few meters to hundreds of meters and temporal scales from minutes to several tens of minutes. Microscale processes directly impact many Army applications—environmental stress factors for Soldiers' operation; atmospheric transport and diffusion; electro-optical (EO) propagation; and operations involving manned and unmanned aircraft. This project seeks to fill an operational gap in weather forecasting by developing a numerical model uniquely suited for forecasting in the microscale, an important setting for the Army. This report details the initial results of what is a long and significant development process.

Currently, there is no microscale community meteorological model available. With the objective of accurate and timely atmospheric prediction for the battlefield and military installations, we have considered some alternatives to address this problem. One alternative is to run a mesoscale model with microscale temporal and spatial resolution. However, state-of-the-art numerical weather prediction (NWP) models are designed to resolve the *mesoscale* (from one to tens of km and one to several hours) up to regional scale. Mesocale NWP models deal with larger weather features and systems such as fronts, strong storms, and precipitation. Those mesoscale models cannot simulate fine-scale wind circulations and other environmental factors due to their neglect of fine-scale topography such as small hills, buildings, and forests in the atmospheric boundary layer (ABL). The physical parameterizations for microscale atmospheric motion are also different from those used in mesoscale models (Wyngaard, 2004; Muschinsky et al., 2004). Moreover, as NWP models move to finer resolution grids, the terrain-following coordinate in the mesoscale models becomes problematic. The vertical coordinate used by most mesoscale models is not designed to handle the sharp variations of the resolved surface features. On the other hand, currently available high-resolution, computation fluid dynamics (CFD) models are mostly developed for specific industrial usages, and therefore, lack important atmospheric processes such as turbulent transport between soil, urban, vegetation, and/or surface water and the atmosphere and radiation. We seek to fill a gap in Army capabilities by developing a prognostic, physics-based, microscale model optimized for use in the ABL. Furthermore, we hope to transition the Atmospheric Boundary Layer Environment (ABLE) model to a real-time prediction tool as future computers become more powerful.

In last several years, we have developed a three-dimensional wind field model (3DWF) for application over complex terrain and in urban settings (Wang et al. 2005; Wang et al. 2010; Hanna et al. 2011). Although a diagnostic type model such as 3DWF is reasonably accurate for strong and neutral wind conditions and consumes very little computing power, it does not model other needed atmospheric variables (i.e., temperature, moisture, and radiation) and has intrinsic shortcomings in dealing with convective and stable conditions. For these reasons, we have

initiated a new project in FY2012 to develop a next generation microscale meteorological model, the ABLE model, to meet the Army application requirements for characterizing the microscale motion of the atmospheric boundary layer. The ABLE model is planned to be an advanced microscale meteorological model that couples the multiple atmospheric environmental variables such as wind, temperature, moisture, and scalars or pollutant transports. The model is based on a set of three-dimensional, prognostic, incompressible, Navier-Stocks equations with special attention given to the microscale variation of atmospheric variables caused by complex boundaries such as buildings, forest canopies, and complex terrain. The model will take advantage of recent developments in the treatment of boundary conditions, computational grid generation, numerical solvers, and turbulence modeling. This model will be a large leap forward in our capability to model the microscale ABL variables and their interactions.

2. Governing Equations

2.1 Mean Atmospheric Variables

The proposed new microscale model will focus on the flows in the ABL. There are several special considerations for a microscale meteorological model. The framework for the ABLE model is based on the following conservation equations for the meteorological variables, including wind, temperature, pressure, scalars such as moisture or pollutant concentrations, and energy transfer between the Earth's surface and the atmosphere. We use a set of incompressible Navier-Stocks system equations with the Boussinesq approximation to eliminate sound waves that have no meteorological significance. The advantage of not resolving sound waves is that the model time marching scheme will allow a much larger time step according to the Courant–Friedrichs–Lewy (CFL) criteria. The Coriolis force is rationally neglected because the domain that this model intends to cover is very small and the Coriolis force is several orders of magnitude smaller than other forces. The choice of this equation set is justified because we are modeling very fine-scale atmospheric motions in the ABL where deep moist convection is not present (Stull 1989; Durran 2008). The first stage in the development is focused on the Reynolds Averaged Navier-Stocks (RANS) type model, and the second stage of the development is extended to the Large Eddy Simulation (LES) type of model. In derivation of the following model equations, two operations were performed for the meteorological variables. The first step is to represent the variables of pressure, temperature, and density as the sum of their base states and deviations. The density deviation from inertial terms are all neglected except in the gravity terms, and the ratio of density deviation to the base density is then replaced with the ratio of potential temperature deviation to the base state potential temperature in the gravity term (i.e., Boussinesq approximation). The second step separates the velocity, potential temperature, and the scalar variables into the two parts, the mean and the turbulent, by ensemble averaging (for RANS) or spatial filtering (for LES). The detailed derivations of the model equation set can be

found in reference books (Stull 1989; Wyngaard 2010). The following is the RANS equation set that is written in conservative tensor form in the Cartesian coordinate:

$$\frac{\partial U_j}{\partial x_j} = 0 \tag{1}$$

$$\frac{\partial(\rho U_i)}{\partial t} + \frac{\partial(\rho U_i U_j)}{\partial x_j} = -\frac{\partial P}{\partial x_i} + \nu \frac{\partial^2 U_i}{\partial x_j^2} + \delta_{i3} \frac{g\theta}{\theta_0} - \frac{\partial(\rho \overline{u_i' u_j'})}{\partial x_j} \tag{2}$$

$$\frac{\partial(\rho \theta)}{\partial t} + \frac{\partial(\rho U_j \theta)}{\partial x_j} = \nu_\theta \frac{\partial^2 \theta}{\partial x_j^2} - \frac{1}{C_p}\frac{\partial R_n}{\partial x_j} - \frac{L_v E}{C_p} - \frac{\partial(\rho \overline{u_j' \theta'})}{\partial x_j} \tag{3}$$

$$\frac{\partial(\rho C)}{\partial t} + \frac{\partial(\rho U_j C)}{\partial x_j} = \nu_c \frac{\partial^2(\rho C)}{\partial x_j^2} - \frac{\partial(\rho \overline{u_j' c'})}{\partial x_j} + S \tag{4}$$

$$C_g \frac{\partial T_g}{\partial t} = R_n - L_v E - H + H_m \tag{5}$$

where U_i and U_j are the ensemble averages of wind velocity components; prime terms are the turbulent fluctuations of the variables; over-bar terms are the turbulent flux or Reynolds stress terms; ρ and θ_0 are the base references of air density and potential temperature; C is the mean scalar mass mixing ratio and the scalar that can be moisture or other gases; and P and θ are the pressure and potential temperature deviations from the base state. The averaged turbulent flux terms of momentum, heat, and scalar parameters are represented by the over bar of primed terms. T_g, R_n, E, H, H_m are the ground surface temperature, net radiation flux, evaporation, sensible heat, and molecular heat conduction between the atmosphere and the ground surface, respectively; ν, ν_θ, ν_c are the dynamic molecular viscosity, diffusivity of heat, and diffusivity of scalar parameters, respectively; C_p, C_g, L_v, S are the specific heat of air at constant pressure, the heat capacity of the Earth surface materials, the latent heat of evaporation, and source strength term for scalar parameters, respectively; and δ_{i3} is the Kronecker delta for tensor notation. The conservation of mass, momentum, energy, scalar parameters, and radiation flux are governed by the equations 1–5, respectively, in tensor differential form. Note that absolute pressure is of no significance, only the pressure gradient affects the flow in the incompressible flow. The pressure field is governed by a Poisson equation, which can be derived by using the pressure-velocity coupling to satisfy the continuity equation.

2.2 Turbulence Closure Models

There are many turbulence closure models that have been developed for different flows. In this section, we only introduce the standard k-ε model and the LES model. This subject will be described in detail once we complete the implementation of a turbulent parameterization in the ABLE model.

2.2.1 k-ε model

In the RANS-type turbulence model, the turbulent fluxes result from partitioning total velocity variables into fluctuation and mean parts via either time or ensemble averages. The turbulent fluxes are computed using the turbulent viscosity, which is analogous to molecular viscosity in the laminar flow. In the k-ε model (Launder and Spalding 1974), the turbulent viscosity (K_m) is determined by the turbulent kinetic energy $(k = \overline{u_i' u_i'}/2)$ and dissipation rate (ε) by

$$K_m = C_\mu \frac{k^2}{\varepsilon}, \tag{6}$$

where C_μ is an empirical coefficient. The turbulent viscosities for heat and scalar, K_h, and K_c, are related to the K_m via the effective Prandtl number ($\mathrm{Pr} = K_m / K_h = 0.7$) and Schmidt number ($\mathrm{Sc} = K_m / K_c = 0.9$). The turbulent kinetic energy (k) and turbulent dissipation rate (ε) are computed using the following prognostic equations:

$$\frac{\partial(\rho k)}{\partial t} + \frac{\partial(\rho U_j k)}{\partial x_j} = -\rho \overline{u_i' u_j'} \frac{\partial U_i}{\partial x_j} - \varepsilon + \frac{\partial}{\partial x_j}\left[(\nu + K_m/\sigma_k)\frac{\partial k}{\partial x_j}\right] + \delta_{j3}\frac{g}{\theta_0}\overline{u_j'\theta'} \tag{7}$$

$$\frac{\partial(\rho \varepsilon)}{\partial t} + \frac{\partial(\rho U_j \varepsilon)}{\partial x_j} = -C_{\varepsilon 1}\rho \overline{u_i' u_j'} \frac{\partial U_i}{\partial x_j} - C_{\varepsilon 2}\frac{\varepsilon^2}{k} + \frac{\partial}{\partial x_j}\left[(\nu + K_m/\sigma_\varepsilon)\frac{\partial \varepsilon}{\partial x_j}\right] + C_{\varepsilon 1}\frac{\varepsilon}{k}\delta_{j3}\frac{g}{\theta_0}\overline{u_j'\theta'} \tag{8}$$

where the numerical values of closure coefficients are taken as follows:

$$C_{\varepsilon 1} = 1.44, \ C_{\varepsilon 2} = 1.92, \ C_\mu = 0.09, \ \sigma_k = 1.0, \ \sigma_\varepsilon = 1.3$$

Launder and Spalding (1974) were the first ones that constructed a numerical model and used above closure coefficients. Detail derivation of above k and ε equations can be found in Wilcox (2006). The physical interpretations of the terms in the turbulent kinetic energy (TKE) equation 7 are as follows. The terms on the left hand are the tendency and advection of TKE by mean flow. The first and last terms on the right-hand side represent the shear and buoyancy production of the TKE, and the third term represents the transport of TKE due to molecular diffusion and turbulence.

The turbulent fluxes terms in the governing equations 2–4 are parameterized with the resolvable mean variables using the Boussinesq's turbulent viscosity approach:

$$\overline{u_i' u_j'} = \frac{2}{3}\delta_{ij}k - K_m\left(\frac{\partial U_i}{\partial x_j} - \frac{\partial U_j}{\partial x_i}\right) \tag{9}$$

$$\overline{u_j'\theta'} = -K_h\frac{\partial \theta}{\partial x_j} \tag{10}$$

$$\overline{u'_j c} = -K_c \frac{\partial C}{\partial x_j} \tag{11}$$

where k is the turbulent kinetic energy. K_m, K_h, and K_c are the turbulent (eddy) viscosities of momentum, heat, and scalar, respectively.

2.2.2 Large Eddy Simulation

In a LES model, the variables are partitioned into a grid resolvable part and a spatial filtered fluctuation part. The LES is a modeling technique to resolve the large, energy containing turbulent eddies and the subgrid turbulent fluxes are parameterized using either an eddy viscosity model or a dynamical model (Smagorinsky 1963; Germano et al. 1990). The model grids have to be smaller than the large eddies to resolve them. Since the scales of the large eddies in many ABL flows are quite small, the computation grids are much finer than RANS-type modeling. The LES requires much more computational power compared with the RANS. We defer description of the LES modeling to the future in the ABLE model development processes. Detail discussion about LES can be found in Pope (2000) and Wyngaard (2010).

3.   Numerical Methods for the Model

3.1   The Structured, Collocated Computational Grid

A box (hexahedron) shaped, structured computational grid is employed in the ABLE model. The rationale to choose the structured box-type grid is that generation of this type of grid is much simpler than generating the unstructured body-fitted grid. With recent research and development of immersed boundary (IB) methods (Mittal and Iaccarino 2005; Tseng and Ferziger 2003), the complex boundary can be treated with the box-type structured grid, which significantly reduces computation time and complexity. The body-fitted computational grid generation is a laborious process often taking several days for a complex terrain (e.g., small urban setting), but the box-type structured grid would generated within a minute for the same computational domain. There are other incentives for using the box-type structured grid in the computation, including (1) less computational time required for one iteration on the structured grid in comparison with the unstructured grid; and (2) the stability of the numerical algorithm on the structured grid being essentially higher than on the unstructured grid (Tseng and Ferziger 2003).

A finite volume (FV) method is used to discretize the model equations. The FV has an advantage over finite difference methods for satisfying mass conservation automatically without special treatments. In this model, the FV sizes are variable to accommodate the resolution requirement in different situations. For an example, much denser grids might be needed to deal with the large gradient of environmental variables to achieve the desired accuracy near the ground surfaces or buildings. Figure 1 shows an arbitrary control volume used to derive the discretized numerical

5

equations for the model. The center of this FV is denoted by the point P, and the uppercase letters, E,W,N,S,T, and B represent the neighboring FVs' centers at east, west, north, south, top, and bottom, respectively. The lowercase letters, e,w,n,s,t, and b represent the locations that are half-distance points from the P to neighboring FVs' centers. The ABLE model also uses a collocated grid for different environmental variables, i.e., all the variables are solved in the same location denoted as P for a control volume. The collocated grid offers various advantages compared with the traditional staggered grid arrangement. This collocated grid setup saves computational time and memory by using the same geometric parameters for the different variables. The collocated grid allows for a single set of common grid geometric parameters reducing computational and memory requirements. It also offers great deal of convenience in boundary treatment for different variables since all variables coincide with the boundary of physical boundaries of the solution domain. The property of the collocated grid offers a great deal of simplicity in treatment of boundary when the IB method is used. The collocated grid requires a special interpolation scheme (Rhie and Chow 1983) to prevent the oscillating velocity and pressure fields, which is described later.

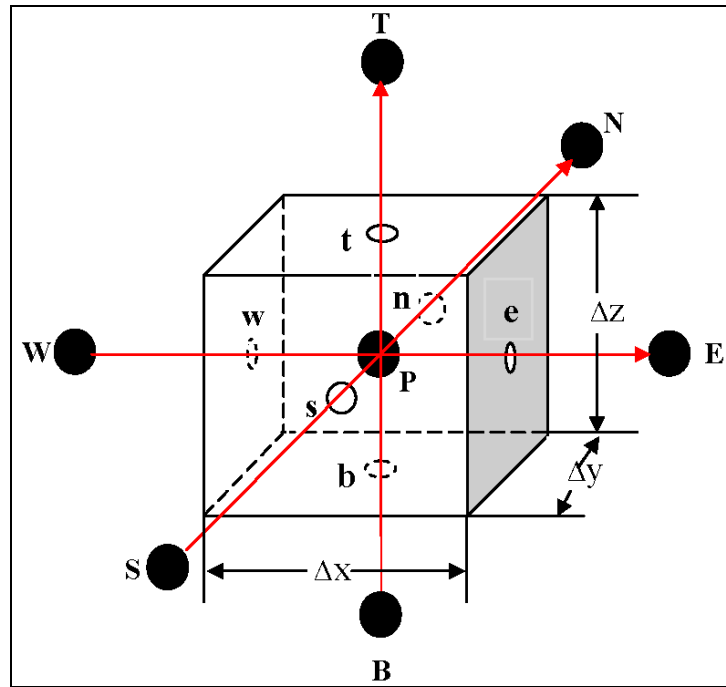Figure 1. A finite volume stencil for ABLE model. The symbol P is the center point that the FV represents, and E, W, S, N, T, B represent the centers of the neighboring FVs. The lowercase letters e, w, s, n, t, b represent the center points on the each faces of the FV P. The geometric length of the FV (ΔX, ΔY ΔZ) can be variable for non-uniform structured computational grid.

3.2 Numerical Method for Scalar Transport Equation

The scalar transport equation is used to demonstrate the numerical discretization without losing the generality for other governing equations, since the momentum and heat transport equations are very similar to scalar transport except the pressure and source terms. The treatment of the pressure gradient force in the momentum equation is described separately. Following Patankar (1980), the scalar transport equation, including the turbulence transport parameterization, can be written in following form:

$$\frac{\partial(\rho C)}{\partial t}+\frac{\partial}{\partial x}\rho\left[UC-(\nu_c+K_c)\frac{\partial C}{\partial x}\right]+\frac{\partial}{\partial y}\rho\left[VC-(\nu_c+K_c)\frac{\partial C}{\partial y}\right]+\frac{\partial}{\partial z}\rho\left[WC-(\nu_c+K_c)\frac{\partial C}{\partial z}\right]=S, \quad (12)$$

where *U, V, W* are three Cartesian components of the wind velocity and *S* is the source strength term for the scalar. Using an implicit time differencing scheme, the integration of this equation over a box-shaped control volume (figure 1) gives

$$\frac{\rho(C_P^{m+1}-C_P^m)\Delta x\Delta y\Delta z}{\Delta t}+\Phi_e-\Phi_w+\Phi_n-\Phi_s+\Phi_t-\Phi_b=S\Delta x\Delta y\Delta z, \quad (13)$$

where superscript *m* denote the values from last outer iteration (time marching), $\Delta x, \Delta y, \Delta z$ are the finite control volume side lengths in the *x, y*, and *z* directions, which are prescribed at different spatial locations for a non-uniform grid configuration. Mass fluxes Φ_{cv_faces} through the faces of the control volumes are

$$\Phi_e=\rho\left[UC-(\nu_c+K_c)\frac{\partial C}{\partial x}\right]_e\Delta y\Delta z,$$

$$\Phi_w=\rho\left[UC-(\nu_c+K_c)\frac{\partial C}{\partial x}\right]_w\Delta y\Delta z,$$

$$\Phi_n=\rho\left[VC-(\nu_c+K_c)\frac{\partial C}{\partial x}\right]_n\Delta x\Delta z,$$

$$\Phi_s=\rho\left[VC-(\nu_c+K_c)\frac{\partial C}{\partial y}\right]_s\Delta x\Delta z,$$

$$\Phi_t=\rho\left[WC-(\nu_c+K_c)\frac{\partial C}{\partial z}\right]_t\Delta x\Delta y,$$

$$\Phi_b=\rho\left[WC-(\nu_c+K_c)\frac{\partial C}{\partial z}\right]_b\Delta x\Delta y. \quad (14)$$

These terms incorporate both the advection and diffusive fluxes through the each of the control volume's faces. Note that the mass flux ρU uses the U values from last outer iteration m. The mass mixing ratio of scalar, C, is at the time step $m+1$ since the implicit scheme is applied to allow the large time steps without numerical instability problem. The superscript of the time step $m+1$ is abbreviated for clarity in the derivation. The continuity equation is satisfied in the scalar transport equation. The advection air mass fluxes, F_i, are determined by the upstream mass fluxes (i.e., $F_e = \rho U_e^m \Delta y \Delta z$) using the velocity values from last outer iteration, named as upstream difference scheme (UDS). The upwind mass flux for scalar is denoted in Q^{UDS}:

$$Q_e^{UDS} = \rho(UC)_e \Delta y \Delta z = C_P \max(F_e,0) - C_E \max(-F_e,0) = C_P \max(F_e,0) + C_E \min(F_e,0)$$

$$Q_w^{UDS} = \rho(UC)_w \Delta y \Delta z = C_W \max(F_w,0) - C_P \max(-F_w,0) = C_W \max(F_w,0) + C_P \min(F_w,0)$$

$$Q_n^{UDS} = \rho(VC)_n \Delta x \Delta z = C_P \max(F_n,0) - C_N \max(-F_n,0) = C_P \max(F_n,0) + C_N \min(F_n,0)$$

$$Q_s^{UDS} = \rho(VC)_s \Delta x \Delta z = C_S \max(F_s,0) - C_P \max(-F_s,0) = C_S \max(F_s,0) + C_P \min(F_s,0)$$

$$Q_t^{UDS} = \rho(WC)_t \Delta x \Delta y = C_P \max(F_t,0) - C_T \max(-F_t,0) = C_P \max(F_t,0) + C_T \min(F_t,0)$$

$$Q_b^{UDS} = \rho(WC)_b \Delta x \Delta y = C_B \max(F_b,0) - C_P \max(-F_b,0) = C_B \max(F_b,0) + C_P \min(F_b,0) \quad (15)$$

To achieve second-order accuracy, we use the deferred correction approach (Khosla and Rubin, 1974, Ferziger and Peric, 2002) to compute the advective mass flux for scalar, which includes the central difference scheme (*CDS*). For the mass flux through the face e of CV,

$$Q_e = Q_e^{UDS} + (Q_e^{CDS} - Q_e^{UDS})^m . \quad (16)$$

The superscript m again means that computation of those fluxes using the last outer iteration solved value. The outcome of the outer iteration is that *UDS* contribution is canceled out, leaving a *CDS* solution which is the second-order accuracy. The *CDS* computation of scalar mass flux is defined as

$$Q_e^{CDS} = Q_E \, r_e + Q_P (1 - r_e) \quad (17)$$

where $r_e = (x_e - x_P)/(x_E - x_P)$, $Q_E = \rho U_E C_E \Delta y \Delta z$, and the lowercase subscripts represents the advective fluxes at the corresponding faces of control volume and the uppercase subscript of C denote the concentration values at the control volume centers. The concentration gradients in each direction are discretized in following central differentials for the computation of diffusive fluxes:

$$\left(\frac{\partial C}{\partial x}\right)_e = \frac{C_E - C_P}{x_E - x_P}, \quad \left(\frac{\partial C}{\partial x}\right)_w = \frac{C_P - C_W}{x_P - x_W}, \quad \left(\frac{\partial C}{\partial y}\right)_n = \frac{C_N - C_P}{y_N - y_P}, \quad \left(\frac{\partial C}{\partial y}\right)_s = \frac{C_P - C_N}{y_P - y_N},$$

$$\left(\frac{\partial C}{\partial z}\right)_t = \frac{C_T - C_P}{z_T - z_P}, \quad \left(\frac{\partial C}{\partial z}\right)_b = \frac{C_P - C_B}{z_P - z_B}. \tag{18}$$

Here we only show $\Phi_e - \Phi_w$ flux in x direction, the fluxes in other two (y and z) directions are similar. Let $D = \rho(\nu_c + K_c)$ be the total diffusion coefficient for a scalar, then

$$\Phi_e - \Phi_w = \rho\left[CU\Delta y\Delta z - D\frac{\partial C}{\partial X}\Delta y\Delta z\right]_e - \rho\left[CU\Delta y\Delta z - D\frac{\partial C}{\partial X}\Delta y\Delta z\right]_w$$

$$= \left[C_P \max(F_e,0) - C_E \max(-F_e,0) - \frac{D\Delta y\Delta z(C_E - C_P)}{x_E - x_P}\right] - \left[C_W \max(F_w,0) - C_P \max(-F_w,0) - \frac{D\Delta y\Delta z(C_P - C_W)}{x_P - x_W}\right]$$

$$= C_E\left[\min(F_e,0) - \frac{D\Delta y\Delta z}{x_E - x_P}\right] + C_W\left[-\max(F_w,0) - \frac{D\Delta y\Delta z}{x_P - x_W}\right] +$$

$$+ C_P\left[F_e - F_w + \max(F_e,0) + \frac{D\Delta y\Delta z}{x_E - x_P} + \max(F_w,0) + \frac{D\Delta y\Delta z}{x_P - x_W}\right] \tag{19}$$

$$= a_E C_E + a_W C_W + C_P(-a_E - a_W + F_e - F_w)$$

Adding the diffusive and advective fluxes in y and z directions and after some simple algebra manipulations, the discretized scalar transport equation can be written as following liner system equations:

$$a_P C_P + a_E C_E + a_W C_W + a_N C_N + a_S C_S + a_T C_T + a_B C_B = b + Q, \tag{20}$$

where

$$a_E = \min(F_e,0) - \frac{(\nu_c + K_c)}{x_E - x_P}\Delta y\Delta z$$

$$a_W = -\max(F_w,0) - \frac{(\nu_c + K_c)}{x_P - x_W}\Delta y\Delta z$$

$$a_N = \min(F_n,0) - \frac{(\nu_c + K_c)}{y_N - y_P}\Delta x\Delta z$$

$$a_S = -\max(F_s,0) - \frac{(\nu_c + K_c)}{y_P - y_S}\Delta x\Delta z$$

$$a_T = \min(F_t,0) - \frac{(\nu_c + K_c)}{z_T - z_P}\Delta x\Delta y$$

$$a_B = -\max(F_b, 0) - \frac{(v_c + K_c)}{z_P - z_B} \Delta x \Delta y$$

$$b = S\Delta x \Delta y \Delta z + a_P^t \, C_P^t$$

$$a_p = a_P^t - a_E - a_W - a_N - a_S - a_T - a_B + (F_e - F_w) + (F_n - F_s) + (F_t - F_b)$$

At this point, the continuity equation 1 can be written in similar finite volume form:

$$F_e - F_w + F_N - F_S + F_T - F_B = 0 \tag{21}$$

Therefore, combining the equations 20 and 21, we have

$$a_p = a_P^t - a_E - a_W - a_N - a_S - a_T - a_B \tag{22}$$

In equation 20, $Q=Q_e+Q_w+Q_n+Q_s+Q_t+Q_b$ is the sum of source terms of advection in each direction due to the deferred correction when using old wind speed values from the last iteration (*t*). (The diffusion source term is neglected.) For example, the deferred flux at e of CV is expressed as

$$Q_e = [(Q_e)^{UDS} - (Q_e)^{CDS}]^m \tag{23}$$

Deferred mass fluxes at other faces of the CV can be computed in the same way.

3.3 Numerical Method for Momentum Transport Equations

Comparing equation 2 with the scalar transport equation 4, besides the terms of change of momentum with time, advection and diffusion in both equations, there are two more terms—the pressure gradient and the gravity in the momentum equations. The momentum equations 2 differ from passive scalar transport equation 4 in two important ways: the momentum equation is nonlinear in advection terms and coupled between all the velocity components so that the equation must be solved iteratively; and the pressure gradient forces require solving the pressure field. The discretization for the advection and the diffusion terms are the same as for the scalar transport. The pressure gradient and gravity terms need special treatment. The discretized algebraic equation for equation 2 is similar to the scalar transport equation except the extra pressure and buoyancy terms. The velocity components from last outer iteration are also used to determine the convective and diffusive mass fluxes. Without repeating much of the derivation for the scalar equation, the discretized momentum equations can be written as follows for U, V, and W components:

$$a_P^U U_P^* = \sum a_{nb}^U U_{nb}^* - \frac{\partial P^*}{\partial x} \Delta x \Delta y \Delta z + SU$$

$$a_P^V V_P^* = \sum a_{nb}^V V_{nb}^* - \frac{\partial P^*}{\partial y} \Delta x \Delta y \Delta z + SV$$

$$a_P^W W_P^* = \sum a_{nb}^W W_{nb}^* - \frac{\partial P^*}{\partial z} \Delta x \Delta y \Delta z + SW \tag{24}$$

Note that in above algebraic equation, we used superscript '*' for *U, V, W*, and *P*. This notation is used for the convenience of the description of the pressure-velocity coupling in the iteration algorithm discussed in the next section. The *nb* represents all the six neighbor points, E, W, N, S, T, B (figure 1) surrounding to the point P. The *SU, SV, SW* are source terms. Since we use the collocated grids, the pressure term need to be interpolated to the location of the control volume faces as denoted in the above equation. Recall that only the deviations of the pressure from the base state contribute to the momentum transport, as stated in basic equation section. The computation for those coefficients is the same as in the discretized scalar equation. The last terms on the above equations are the source terms including the buoyancy, turbulent diffusion, and deferred correction in the inner iteration.

3.3.1 Pressure-velocity Coupling in the Outer Iteration

In the incompressible equation set, there is no independent equation for pressure (thermodynamic pressure is undefined). Instead, the pressure gradient forcing is calculated by taking the divergence of the momentum equation 2, using the incompressible continuity equation 1, and assuming the constant density and viscosity to produce the following Poisson equation for pressure:

$$\frac{\partial^2 P}{\partial x_i^2} = -\frac{\partial}{\partial x_i}\left[\frac{\partial(\rho U_i U_j)}{\partial x_j}\right] \tag{25}$$

Note that the absolute pressure value is not needed; only the gradient of the pressure is important in incompressible flow. The pressure deviation contributes to the pressure gradient force. The pressure and velocity are not solved simultaneously; rather, they are solved by an iterative process. In the Semi-Implicit Method for Pressure-Linked Equations (SIMPLE) iteration (Patankar, 1980), pressure and velocity are corrected by adding the correction parts (denoted by superscript ′) for the variables solved in last outer iteration (denoted by superscript *), i.e.,

$$\begin{aligned} P &= P^* + P' \\ U &= U^* + U' \\ V &= V^* + V' \\ W &= W^* + W' \end{aligned} \tag{26}$$

The corrected velocities can be similarly expressed as equation 24:

$$a_P^U U_P = \sum a_{nb}^U U_{nb} - \frac{\partial P}{\partial x} \Delta x \Delta y \Delta z + SU$$

$$a_P^V V_P = \sum a_{nb}^V V_{nb} - \frac{\partial P}{\partial y} \Delta x \Delta y \Delta z + SV$$

$$a_P^W W_P = \sum a_{nb}^W W_{nb} - \frac{\partial P}{\partial z} \Delta x \Delta y \Delta z + SW \qquad (27)$$

Subtracting the equations 24 from equations 27, an equation set for correction terms is derived:

$$a_P^U U'_P = \sum a_{nb}^U U'_{nb} - \frac{\partial P'}{\partial x} \Delta x \Delta y \Delta z$$

$$a_P^V V'_P = \sum a_{nb}^V V'_{nb} - \frac{\partial P'}{\partial y} \Delta x \Delta y \Delta z$$

$$a_P^W W'_P = \sum a_{nb}^W W'_{nb} - \frac{\partial P'}{\partial z} \Delta x \Delta y \Delta z \qquad (28)$$

The SIMPLE procedure estimates the above equations by omitting $\sum a_{nb}^U U'_{nb}$, $\sum a_{nb}^V V'_{nb}$, and $\sum a_{nb}^W W'_{nb}$ terms. Since this is an iteration procedure, it is a valid approximation. The detailed discussion can be found in Patankar (1980) and Tu et al. (2008). Substituting the equations 28 without those $\sum$ terms, the simplified equation can be written as

$$U_P = U_P^* - B^U \frac{\partial P'}{\partial x}$$

$$V_P = V_P^* - B^V \frac{\partial P'}{\partial y}$$

$$W_P = W_P^* - B^W \frac{\partial P'}{\partial z}, \qquad (29)$$

where $B^U = \Delta x \Delta y \Delta z / a_P^U$, $B^V = \Delta x \Delta y \Delta z / a_P^V$, $B^W = \Delta x \Delta y \Delta z / a_P^W$. By summing up the three equations in equation 29, taking the divergence of the resulted summation, and using the continuity equation, the equation for P′ is derived:

$$\frac{\partial}{\partial x}\left(B^U \frac{\partial P'}{\partial x} \right) + \frac{\partial}{\partial y}\left(B^V \frac{\partial P'}{\partial y} \right) + \frac{\partial}{\partial z}\left(B^W \frac{\partial P'}{\partial z} \right) = \frac{\partial U^*}{\partial x} + \frac{\partial V^*}{\partial y} + \frac{\partial W^*}{\partial z} \qquad (30)$$

This Poisson equation can be discretized in similar way as done for the scalar and momentum equation.

One thing that needs to be stressed here is the treatment of pressure and velocity coupling on the collocated grid. The Rhine and Chow (1983) velocity interpolation is used for the wind components at the CV faces to eliminate spurious pressure and velocity oscillations from the collocated grid. In contrast to the simple interpolation of velocity components only, the Rhine

Chow velocity interpolates both the velocity components and the pressure gradient for their CV face values, and adds a higher order correction term for CV face velocity interpolation. This is equivalent to adding a pressure smoothing term that is proportional to the third derivative of the pressure to prevent from occurrence of spurious pressure mode. This interpolation can be expressed as follows for a one-dimensional example:

$$U_e = \frac{1}{2}(U_E + U_P) + \frac{\delta V}{2a_P}\left[\left(\frac{dP}{dx}\right)_E + \left(\frac{dP}{dx}\right)_P\right] - \frac{\delta V}{a_P}\frac{P_E - P_P}{\Delta x} \tag{31}$$

The SIMPLE algorithm is summarized in figure 2. The initial step begins by guessing a pressure P^*, the velocity components, U^*, V^*, W^* can be solved using equation 24. The pressure (P') field then can be solved via Poisson equation, equation 30. At the next step, the pressure and velocity are corrected using equation 26. At this point, by using the corrected velocity components and pressure, the temperature, other scalar variables, and turbulence transport equations can be solved using the velocity and pressure values from the last step. The last step is to check the convergence. If the convergence is not achieved, replace the U^*, V^*, W^* P^* with the newly solved U, V, W, P, and go through another outer iteration.
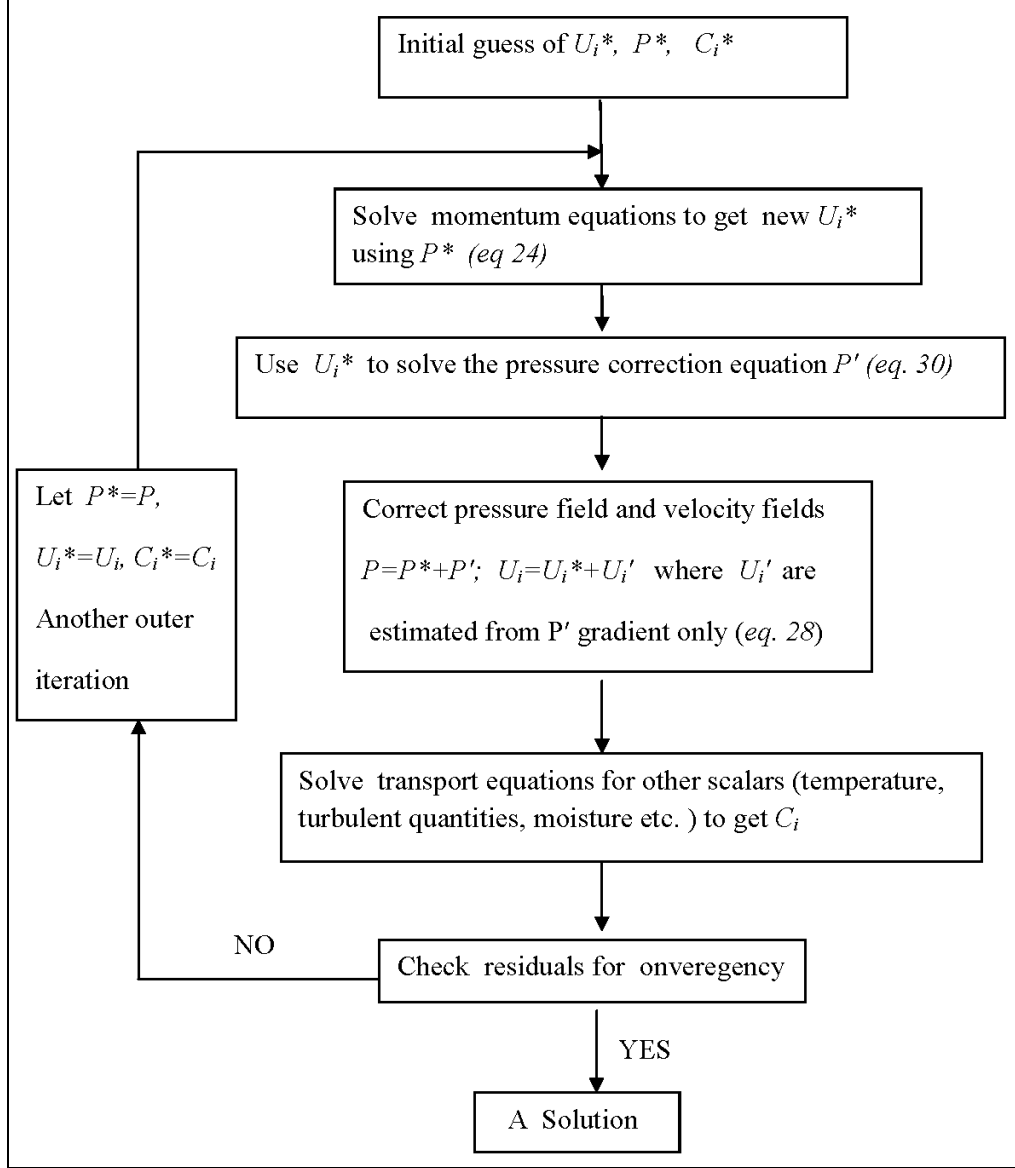
Figure 2. A block diagram for the SIMPLE algorithm.

3.4   Method for Solving the Discretized Algebraic System Equations

After FV discretization, each of the governing equations of wind components, energy, and scalars becomes a set of linear system equations, whose coefficient is a sparse, seven-diagonal matrix. There are several methods to solve this type of system of algebraic equations, the successive over relaxation (SOR) method; the alternate-direction implicit (ADI) method; the strongly implicit procedure (SIP) (Stone, 1968; Leister and Peric, 1994); and the bi-conjugate gradient stabilized (BI-CGSTAB) (Van den Vorst, 1992). Since most computation is in this matrix solver, we will continually evaluate solution methods for the ABLE model based on speed, accuracy, and numerical stability; some experimentation will be required during model development. Terrain, building, and morphology conditions may also alter the performance of

the solvers. For example, a technique might perform better in urban but not mountainous complex terrain. We intend to perform sensitivity tests for these numerical solvers and provide guidance to the user for which options to use when setting up a model run. For the prototype, we choose the SIP method for testing the framework. The SIP method creates an easily factorable matrix operator for iteration. The rate of convergence is increased by adding a contribution based on a smoothness assumption in the dependent variable.

4. Boundary Conditions

The boundary conditions discussed in this section are applied only for the mean conservation equations of momentum, energy, and scalar. The discussion of boundary conditions for turbulent fluxes and TKE equation will be postponed until future development. We also planned to develop an IB method for the ABLE model. The description of IB method will also be deferred to later because it is a large research and development problem.

4.1 Inflow Boundary

The inflow properties must be prescribed at the inflow boundary. The wind components *U, V, W,* and potential temperature can interpolated either from the observational data or from a larger-scale model (e.g., mesoscale numerical prediction model) results. For an unsteady problem, a new inflow velocity value is prescribed at each time step. In the case of fully turbulent flow, a logarithmic wind profile is imposed at the surface layer. For example, in idealized, plane-parallel flow from the west boundary, the U wind profile will be logarithmic while V and W are set to zero.

Since the inflow velocity boundary is prescribed, it should be kept constant during the outer or inner iteration for a steady solution. The pressure correction $P^{'}$ is kept as zero due to the constant inflow velocity in the steady flow at the boundary.

4.2 Outflow Boundary

At an outflow boundary, the zero gradient boundary conditions are set for every variable. For an unsteady flow, the flow variables are also extrapolated according to the zero gradient condition at the outflow boundary.

4.3 Wall Boundary

4.3.1 Wind and Pressure

For momentum equations, a non-slip boundary Dirichlet condition is applied at the walls by setting all velocity components to zero. Besides the non-slip boundary condition, there is another Neumann boundary condition that needs to be applied for the diffusive fluxes terms at the walls (figure 3).
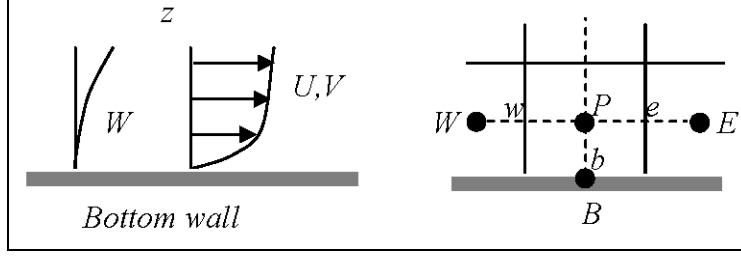
Figure 3. A schematic diagram for the wall boundary.

For a wall boundary, taking a bottom wall as an example,

$$\frac{\partial U}{\partial x} = \frac{\partial V}{\partial y} = \frac{\partial W}{\partial z} = 0 \ , \qquad \frac{\partial U}{\partial z} \neq 0 \ , \qquad \frac{\partial V}{\partial z} \neq 0 \ . \tag{32}$$

The diffusive flux at the bottom wall is then expressed as

$$\int_{S_b} \tau_{xz} dS = \int_{S_b} \mu \frac{\partial U}{\partial z} dS \approx \mu S_b \frac{U_P - U_B}{z_P - z_B} \tag{33}$$

$$\int_{S_b} \tau_{yz} dS = \int_{S_b} \mu \frac{\partial V}{\partial z} dS \approx \mu S_b \frac{V_P - V_B}{z_P - z_B} \tag{34}$$

For this model discretization, we applied collocated the computation grid. All CVs extend to the boundary and boundary pressure is needed to calculate the pressure forces in the momentum equations. A linear extrapolation is applied to obtain the pressure at the boundaries.

4.3.2 Temperature, Thermal Flux from Ground

These boundary conditions will be discussed in future development of the ABLE model.

4.4   Symmetry Plane (Free-slip)

For a symmetry plane or top the computational domain, a symmetry plane can be used to eliminate momentum transport to outside of the domain. In this type of boundary condition, the normal velocity to the symmetry line or plane is zero. Figure 4 is an example of horizontal at top of the boundary layer in three dimensions.
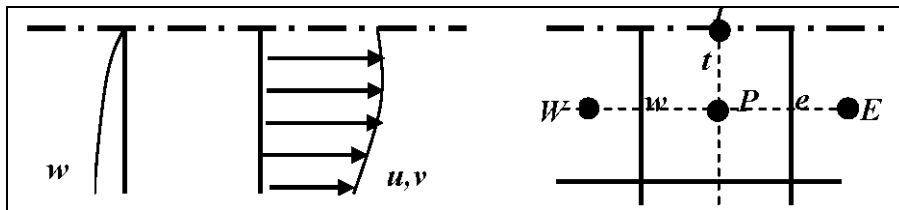

Figure 4. A schematic diagram for top symmetry boundary.

$$\frac{\partial U}{\partial z} = \frac{\partial V}{\partial z} = 0, \quad \frac{\partial W}{\partial z} \neq 0 \tag{35}$$

The diffusive flux at the horizontal symmetry plane is computed as

$$\int_{S_t} \tau_{zz} dS = \int_{S_t} 2\mu \frac{\partial W}{\partial z} dS \approx \mu S_t \frac{W_P - W_T}{z_P - z_T} \tag{36}$$

The boundary conditions are applied for momentum equations in such a way that the flux coefficients for the CV at the boundary are added for the planes of boundary finite volumes.

4.5   Immersed Boundary Conditions

Recently, there has been significant advancement in IB methods. The IB method (Tseng and Ferziger, 2003; Mittal and Iaccarino 2005; Lundquist et al. 2007) has been recognized as one of the most accurate and efficient methods for complex geometry in geophysical flows. The IB method specifies a boundary value in such a way as to simulate the presence of a body surface in a cell without altering the structured computation grid so arbitrary shapes can be handled. This method combined with the structured box type grid will significantly reduce the difficulty in grid generation for very complex lower boundary surface. Because this is a topic that has to be studied and formulated for the ABLE model, we defer the detailed description to the future once we have finished and tested implementation of the method.

5.   Preliminary Results

It is a good practice in the model development process to test the model with some well-known laboratory results or analytical solution. We have done some preliminary tests and compared them with the laboratory results. The first case is a 2-D simulation of the flow past an infinitely long cylinder, in which the well-known lee side vortices are generated. The second case is a 3-D lid-driven cavity flow. Extensive laboratory results are available from the literature for both cases.

5.1   Flow Past a Infinite Long Cylinder

A 2-D test simulation of steady flow past a cylinder is performed. The flow is dependent upon the Reynolds number, $R_e = U_\infty D / \nu$, where D is the diameter of the cylinder, U_∞ is the upstream fluid velocity, and ν is the dynamic viscosity. There are many flow laboratory tests and a visualization database is available. At $R_e < 5$, the flow is a creeping or Stokes flow, in which there is no lee side vortex. At a medium Reynolds number around ($R_e < 50$), two symmetrical standing vortices are formed at the lee side. At a higher Reynolds number, these vortices are stretched and wavy behavior is observed. At an even higher Reynolds number ($R_e > 100$), an

17

alternating vortex shedding from the cylinder at the lee side, called a Von Karman vortex street, is observed.

Preliminary tests for ABLE were performed for R_e=40 and R_e=100. The simulations were performed in a domain (length x width = 40D x 20D) large enough to eliminate the outer boundary effect on the wake formation. The total grid number is 200 x 100. Figure 5 shows the flow at R_e=40, and R_e=100, compared with the images from the album of fluid motion by Van Dyke (1982). Note that the Reynolds number are not exactly the same as in our simulation, but the Re are close enough, i.e., within the same regimes of the flow pattern. The results also compared well with the numerical simulation of Tseng and Ferziger (2003).
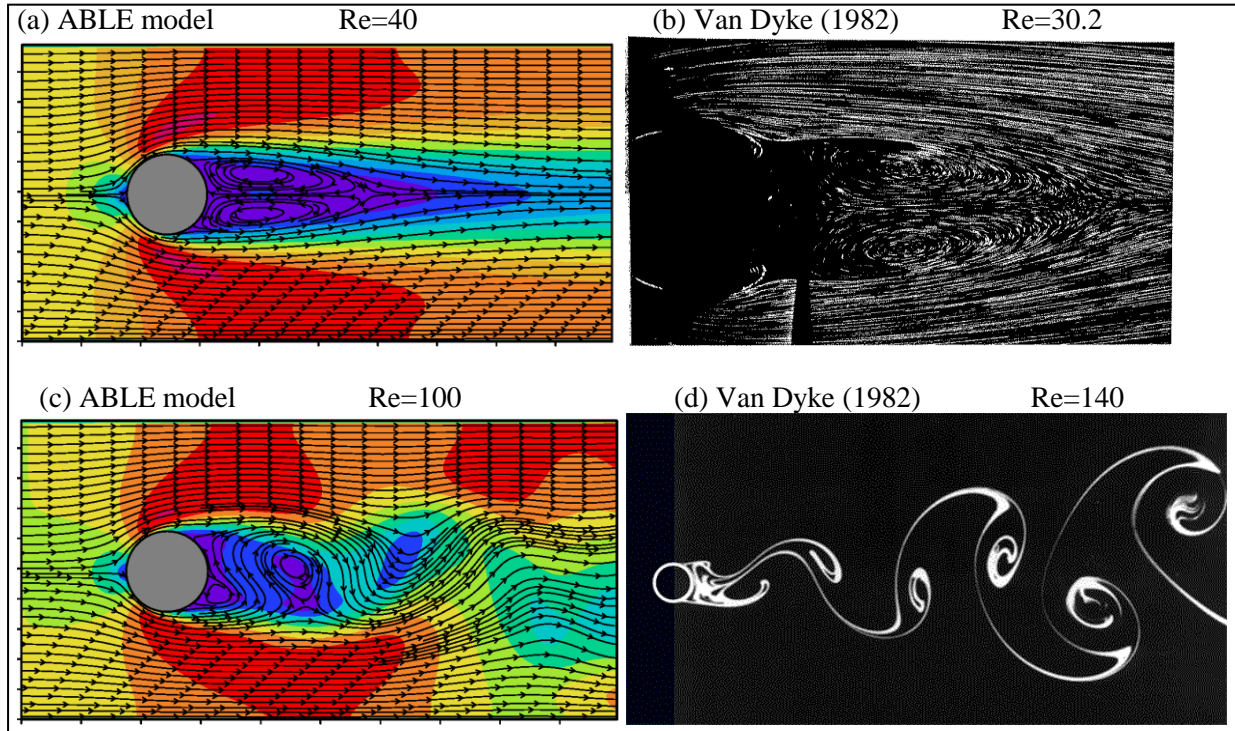

Figure 5. A comparison of the ABLE solution with the laboratory visualization (Adopted from Van Dyke 1982) at different Reynolds numbers.

5.2   Three-dimensional Lid-driven Cavity Flow

This test case is specifically for the 3-D framework of the ABLE model. In this case, a cubic cavity is filled with a fluid and the top cover of the cavity is moved at a steady speed to specify a Reynolds number. Several laboratory test data sets are available with different Reynolds numbers. We use the test results by Parasad and Kosseff (1988) for comparison.

In this simulation, the computational grid is a uniform grid with 100 x 100 x 100 grid points. The Re=3200 was set for the comparison with the laboratory results. For this simple lid-driven cavity flow, the flow showed complex patterns. This result is the steady-state solution for the flow. The results at the different cross sections are shown in figure 6. The ABLE model simulated U and W

components at the center plane at y=1/2W show good agreement with the laboratory test results of Parasad and Kosseff (1989).
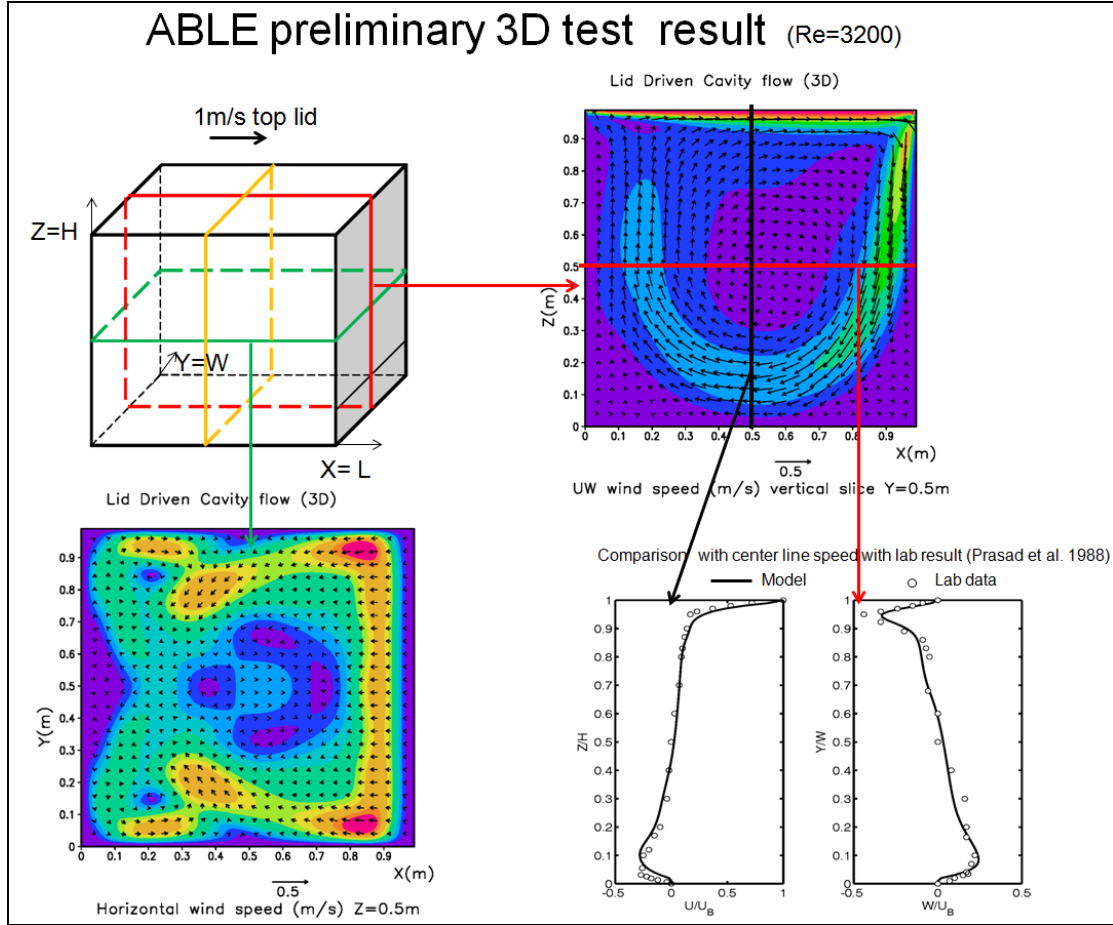

Figure 6. ABLE model simulation of a lid-driven cavity flow. The cross sections denoted from the color-coded planes. The results were compared with the laboratory test data from Prasad and Kosseff (1989).

We have also compared ABLE model results with other numerical simulations. Figure 7 is a plot of symmetry plane (Z-Y) at X=0.75 for VW components from simulations of Zang et al. (1994) and the ABLE model. Taylor-Göertler-like vortices are evident near the Z=0.15. These types of vortices are also observed in the laboratory test (Prasad and Kosseff, 1989). The flow in cubic lid-driven cavity is symmetric at the XY and YZ planes due the boundaries and forces in this flow. This property is also a good check for model code correctness. The results in figures 6 and 7 show this symmetric property.
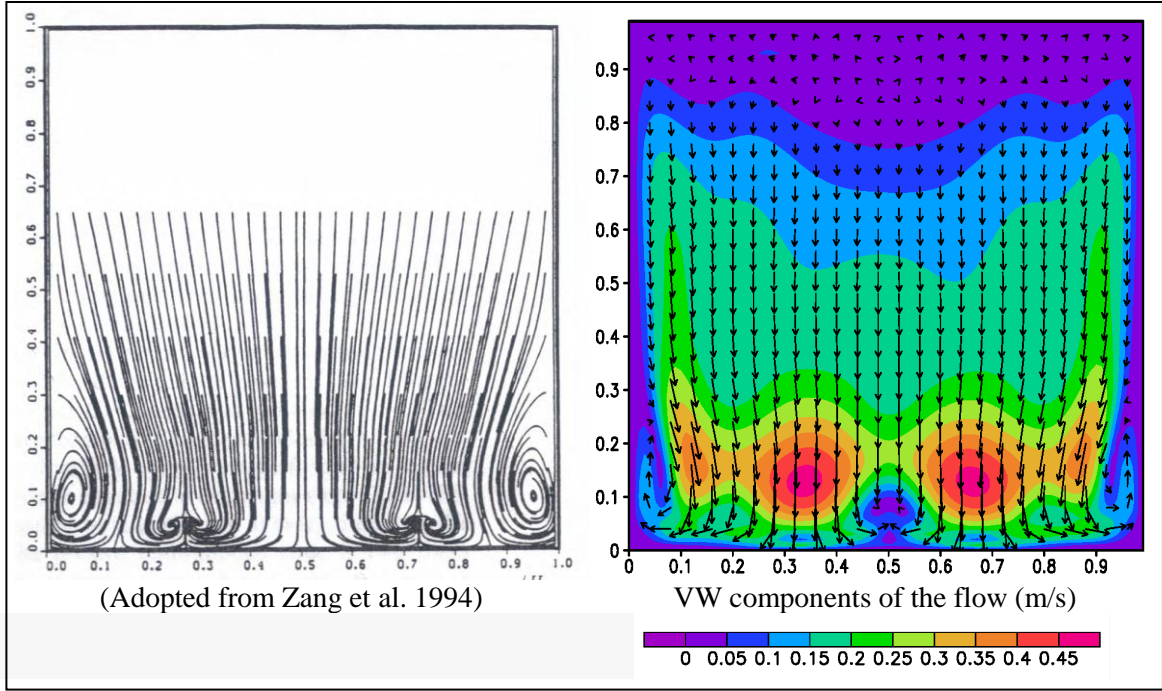
Figure 7. ABLE simulation compared with other numerical model results for the YZ plane at X=0.75. Left panel: streamline from the simulation of Zang et al. (1994). Right panel: the flow field cross section at the same location as Zang et al.

6. Conclusion

A framework for a microscale meteorological model, ABLE, has been developed. A lot of difficult tasks are still ahead of us to enable a complete model. The objective the ABLE model is to simulate microscale (defined meters to hundreds of meters in space and minutes in time) atmospheric processes in the ABL. We have chosen a set of incompressible set of governing equations for the model according to our objectives and intended scope of applications. In this framework, we have used a Cartesian coordinate system, a finite volume approach, and collocated grids for the numerical discretization of the model system. The numerical integration for the scalar and momentum equations is described in detail in the report. The SIMPLE method was selected for the semi-implicit coupling of the velocity and pressure fields. Some simple boundary conditions are discussed and simple test cases are presented in this report. Some planned features for this model system, such as turbulence model for sub-grid scale and the treatment of complex boundary, are also described briefly.

This is the starting point of ABLE model development. Several planned development components of the system, such as IB method for treatment of complex boundary, turbulence parameterization for the ABL flow, radiation and surface energy exchange, and parallelization of the computation, will be carried out in future research and development.

20

7. References

Durran, D. R. A Physically Motivated Approach for filtering Acoustic Waves from the Equations Governing Compressible Stratified flow. *J. Fluid Mech.* **2008**, *601*, 365–379.

Ferziger, J. H.; Peric, M. Computational Methods for Fluid Dynamics, Springer, 2002.

Germano, M.; Piomelli, U.; Moin, P.; Cabot, W. H. A Dynamic Subgrid Scale Eddy Viscosity Model. *Proc. Summer Workshop, Center for Turbulence Research*, Stanford, CA, 1990.

Hanna,S.; White, J.; Trolier,J.; Vernot, R.; Brown, M.; Gowardhan, A.; Kaplan, H.; Alexander, Y.; Moussafir, J.; Wang, Y.; Williamson, C.; Hannan, J.; Hendrick , E. Comparisons of JU2003 Observations with Four Diagnostic Urban Wind Flow and Lagrangian Particle Dispersion Models. *Atmos. Environment* **2011***, 45*, 4073–4081.

Khosla, P. K.; Rubin, S. G. A Diagonally Dominant Second-order Accurate Implicit Scheme. *Computers fluids* **1974**, *2*, 207–209.

Launder, B.; Spalding, D., The Numerical Computation of Turbulent Flows. *Computer Methods in Applied Mechanics and Engineering* **1974**, *3*, 269–289.

Leister, H.-J.; Peric, M. Vectorized Strongly Implicit Solving Procedure for a Seven-Diagonal Coefficient Matrix. *Int. J. Num. Meth. Heat Fluid Flow*. **1994**, *4*, 159–172.

Lilly, D. K. A Comparison of Incompressible, Anelastic and Boussinesq Dynamics. *Atmos. Res.* **1996**, *40*, 143–151.

Lundquist K. A.; Chow, F. K.; Lundquist, J. K.; Mirocha, Jeffery D. Development of an Immersed Boundary Method to Resolve Complex Terrain in Weather Research and Forecasting Model. *7th Symposium on the Urban Environment*, American Meteorological Society, San Diego, 2007.

Mellor, G. L.; Yamada, T. A Hierarchy of Turbulence Closure Models for the Planetary Boundary Layer. *J. Atmos. Sci.* **1974**, *31*, 1791–1806.

Mittal, R.; Iaccrino, G. Immersed Boundary Method. *Annu. Rev. Fluid Mech*. **2005**, *37*, 239–61.

Muschinsky, A.; Frehlich, R. G.; Balsley, B. B. Small-scale and Large-scale Intermittency in the Nocturnal Boundary Layer and the Residual Layer. *Journal of Fluid Mechanics* **2004**, *515*, 319–351.

Patankar, S. V. *Numerical Heat Transfer and Fluid Flow*; Hemisphere Publishing Co: New York, 1980.

Pop, S. *Turbulent Flows*, Cambridge Press, 769 pp, 2000.

Prasad, A. K.; Koseff, J. R. Reynolds Number and End-wall Effects on a Lid-driven Cavity Flow. *Phys. Fluids* A 1, 208, 1989, doi: 10.1063/1.857491.

Smagorinsky, J. General Circulation Experiments with the Primitive Equations. Part I: The Basic Experiment. *Mon. Weather Rev*. **1963**, *91*, 99–164.

Rhie, C. M.; Chow, W. L. Numerical Study of the Turbulent Flow Past an Airfoil with Trailing Edge Separation. *AIAA J.* **1983**, *21*, 1525–1532.

Stone, H. L. Iterative Solution of Implicit Approximations of Multidimentional Partial Differential Equations. *SIAM J. Numer. Anal*. **1968**, 5, 530–558.

Stull, R. B. *An Introduction to Boundary Layer Meteorology*; Kluwer Academic Publishers, 666 pp, 1988.

Tseng, Y. –H.; Ferziger, J. H. A Ghost-cell Immersed Boundary Method for Flow in Complex Geometry. *J. Compu. Physics* **2003***, 192*, 593–623.

Tu, J.; Yeoh, G. H.; Liu, C. *Computational Fluid Dynamics, A Practical Approach*; Elsevier, 459 pp, 2008.

Van den Vorst, H. A. BI-CGSTAB: A Fast and Smoothly Converging Variant of BI-CG for the Solution of Non-symmetric Linear Systems. *SIAM J. Sci. Stat. Comput.* **1992**, *13*, 531–644.

Van Dyke, Milton. *An Album of Fluid Motions*; Parabolic Press Inc.: Stanford, California, 1982.

Wang, Y.; Williamson, C.; Garvey, D.; Chang, S.; Cogan, J. Application of a Multigrid Method to a Mass Consistent Diagnostic Wind Model. *J. Appl. Meteorol*. **2005**, *44*, 1078–1089.

Wang, Y.; Williamson, C.; Huynh, G.; Emmitt, D.; Greco, S. Diagnostic Wind Model Initialization over a Complex Terrain Using the Airborne Doppler Wind Lidar Data. *The Open Remote Sensing Journal* **2010**, *3*, 17–27.

Wilcox, D. C. *Turbulence Modeling for CFD*; Birmingham Press, 515 pp, 2006.

Wyngaard, J. C. *Turbulence in the Atmosphere*; Cambridge Univ. Press, 393 pp, 2010.

Wyngaard, J. C. Toward Numerical Modeling in the "Terra Incognita." *Journal of Atmospheric Sciences* **2004**, *61*, 1816–1826.

Zang, Y.; Street, R. L.; Koseff, J. R. A Non-staggered Grid, Fractional Step Method for Time-dependent Incompressible Navier-Stockes Equations in Curvilinear Coordinates. *J. Computational Physics.* **1994**, *114*, 18–33.

List of Symbols, Abbreviations, and Acronyms

3DWF	Three-dimensional Wind Field
ADI	alternate-direction implicit
ABL	atmospheric boundary layer
ABLE	Atmospheric Boundary Layer Environment
BI-CGSTAB	bi-conjugate gradient stabilized
CV	control volume
CDS	central difference scheme
FV	finite volume
IB	immersed boundary
LES	large eddy simulation
NWP	numerical weather prediction
RANS	Reynolds averaged Navier-Stocks
TKE	turbulent kinetic energy
SOR	successive over relaxation
SIP	strongly implicit procedure
SIMPLE	Semi-Implicit Method for Pressure-Linked Equations
UDS	upstream difference scheme

No. of
Copies   Organization

    1   ADMNSTR
  ELEC   DEFNS TECHL INFO CTR
            ATTN DTIC OCP
            8725 JOHN J KINGMAN RD STE 0944
            FT BELVOIR VA 22060-6218

    3   US ARMY RSRCH LAB
            ATTN IMAL HRA
            MAIL & RECORDS MGMT
            ATTN RDRL CIO LL TECHL LIB
            ATTN RDRL CIO LT TECHL PUB
            ADELPHI MD 20783-1197

    1   US ARMY RSRCH LAB
  ELEC   ATTN RDRL WML B J CIEZAK-JENKINS
            BLDG. 390
            ABERDEEN PROVING GROUND MD
            21005-5069

   13   US ARMY RESEARCH LAB
            ATTN RDRL CIE D
            Y WANG (10 COPIES)
            C WILLIAMSON
            B MACCALL
            ATTN RDRL CIE P CLARK
            ADELPHI, MD

    5   US ARMY RESEARCH LAB
            ATTN RDRL CIE D
            D HOOCK (5 COPIES)
            BLDG 1622
            WHITE SANDS MISSILE RANGE
            NM 88002-5501

TOTAL: 23 (2 ELEC, 21 HCS)